photonics

MDPI

Article

Random Emission and Control of Whispering Gallery Mode Using Flexible Optical Fiber

Bingyang Cao †, Zhen He † and Weili Zhang *

Fiber Optics Research Centre, School of Information and Communication Engineering, University of Electronic Science & Technology of China, Chengdu 611731, China; caobingyang@std.uestc.edu.cn (B.C.); hezhen@std.uestc.edu.cn (Z.H.)

* Correspondence: wl_zhang@uestc.edu.cn

† These authors contributed equally to this work.

Abstract: Axially uniform optical fibers provide a low-cost, scalable platform for the emission of whispering gallery mode (WGM) lasers. This paper proposes a method for generating and controlling WGM lasers based on the design of a flexible optical fiber array structure. By adjusting the spacing between the flexible fibers, the coupling relationship between different WGM modes is modulated, achieving a transition from regular to random WGM (R-WGM) mechanisms. Additionally, the application of this laser in information security encryption is demonstrated and explored.

Keywords: random laser; optical microcavity; mode control

1. Introduction

Optical microcavity lasers, constructed using various micron-sized optical resonators, exhibit strong confinement of light, which significantly enhances the Q factor of the laser and lowers the lasing threshold. It also offers strong mode control and selection capabilities [1–5]. The advantages of controlling the output wavelength, intensity or frequency of microcavity lasers also make them more suitable for application scenarios such as high-speed optical communication, dynamic optical modulation, lidar, laser sensing, and information encryption [6–15]. Meanwhile, the smaller cavity size allows microcavity lasers to be easily integrated into compact optoelectronic devices or photonic chips [16–18].

The whispering gallery mode (WGM) has been widely used in the resonance construction of various microcavities due to its smaller mode size, simpler resonance conditions, higher mode excitation efficiency, and narrow linewidth [19–25]. Among them, fiber-optic WGMs have unique advantages in homogeneous preparation and multidimensional array multiplexing, which have received extensive attention. The resonance of the WGM occurs mainly in the inner wall of the annular-like microcavity, where specific wavelength modes satisfying the resonance conditions undergo total internal reflection on the inner surface of the cavity, forming an internal tangential annular distribution. In combination with the pump gain, suitable modes are continuously amplified in the cavity to obtain emission. The transmission spectra of WGM lasers typically exhibit narrow linewidth resonance peaks and fixed free spectral range (FSR) with strong wavelength and momentum selectivity [26].

check for updates

Received: 27 November 2024
Revised: 20 December 2024
Accepted: 30 December 2024
Published: 1 January 2025

Citation: Cao, B.; He, Z.; Zhang, W. Random Emission and Control of Whispering Gallery Mode Using Flexible Optical Fiber. *Photonics* **2025**, *12*, 29. https://doi.org/10.3390/photonics12010029

Copyright: © 2025 by the authors. Licensee MDPI, Basel, Switzerland. This article is an open access article distributed under the terms and conditions of the Creative Commons Attribution (CC BY) license (https://creativecommons.org/licenses/by/4.0/).

Traditional WGM is a resonant mode of an internally closed system, where the energy in the resonator can only interact with the external environment through the evanescent field at the boundaries, resulting in low gain utilization and coupling output efficiency. To address this issue, researchers have started introducing appropriate defects to break the rotational symmetry of the cavity. This approach improves the utilization of the gain medium while enabling a certain degree of directional coupling output [27–29]. As the disorder is introduced into the cavity, not only does the coupling efficiency increase, but the originally stable resonant modes can also be altered. Some typical WGM modes transform into other unstable resonant modes. Due to multiple scattering and reflection events in irregular cavities, various resonant modes in disordered microcavity lasers continuously compete within the cavity, ultimately leading to the generation of broadband, multi-peak random lasing. This process completes the transition from ordered to disordered systems or from WGM lasers to random lasers.

Exploring the output transition of microcavity lasers from ordered to disordered states is highly meaningful [30]. Firstly, due to the small size of the cavity and the mode volume, microcavity lasers exhibit rich nonlinear dynamical behaviors [31–35]. This provides an important optical tool for studying the evolution of complex events. Furthermore, investigating the transition process in microcavity lasers can help us more flexibly control the operating modes and output characteristics of the laser, injecting new vitality into fields such as laser sensing and laser imaging [36–39]. However, most existing random micro-lasers require precise processing of the cavity walls or the incorporation of specific micron or nanoscale particles to enhance the laser's performance [40–42]. This undoubtedly increases the cost of large-scale applications and makes it difficult to control the degree of randomness in the final laser output (i.e., the boundary between ordered and random outputs is hard to control).

To address the above-mentioned issue, this article proposes a low-cost method for generating and controlling WGM lasers based on designing the array structures of flexible optical fibers (adjust the spacing between the flexible fibers) to regulate the coupling between different WGM modes. This enables the transition from regular WGM to random WGM (R-WGM) mechanisms in a near-macroscopic manner (without the need for molecular-scale doping or surface control). Additionally, a Rivest-Shamir-Adleman (RSA)-based signature authentication algorithm is proposed, making use of the unique characteristics of high randomness and broad bandwidth in the dynamic fluctuations of the output spectra from the R-WGM. This work enriches the study of the complex mechanism of WGM lasers and provides guidance for the development of low-cost arrayed micro-lasers and their applications in information technology.

2. Experimental Setup

The homemade microcavity sample is pumped by a Q-switched frequency-doubled Nd^{3+}:YAG laser at 532 nm with a pulse duration of 6 ns and a repetition frequency of 1 Hz, as shown in Figure 1. The linearly polarized light output from the Nd^{3+}:YAG laser is power-controlled by a polarizer and then split into two parts by a beam splitter with a 1:25 power ratio. The minor part is used for monitoring the pulse power, while the major part is focused by an objective lens and used as the pump light with a spot size of approximately 710 μm illuminate on the sample. The flexible optical fiber (low-cost and low-standard fishing line with a solid core) is made of polyamide (PA) with a diameter $D \approx 60$ μm and an effective refractive index of $n_1 = 1.58$. Several fibers are placed transversely at a certain spacing and fixed at both ends with optical UV glue on a transparent glass plate (the inset of Figure 1). Subsequently, gain solution with lower refractive index ($n_2 \approx 1.36$) is prepared by dissolving 0.3 wt% of the Pyrromethene 597 (PM597) dye powder in 99.8% ethanol and

the fluorescence peak is typically around $\lambda \approx 580$ nm, which is evenly applied to cover the surface of the sample and fill the gaps between the fibers. The maximum evanescent field penetration depth between PA and gain solution is $d_p = \frac{\lambda}{2\pi n_1 \sqrt{sin^2\theta - (n_2/n_1)^2}} \approx 81$ μm ($\theta = \sin^{-1}\left(\frac{n_2}{n_1}\right) \approx 0.30056\pi$ represents the minimum angle of total internal reflection) [43]. Part of the emitted light is measured at the rear using a spectrometer (CHS3000, resolution 0.1 nm).

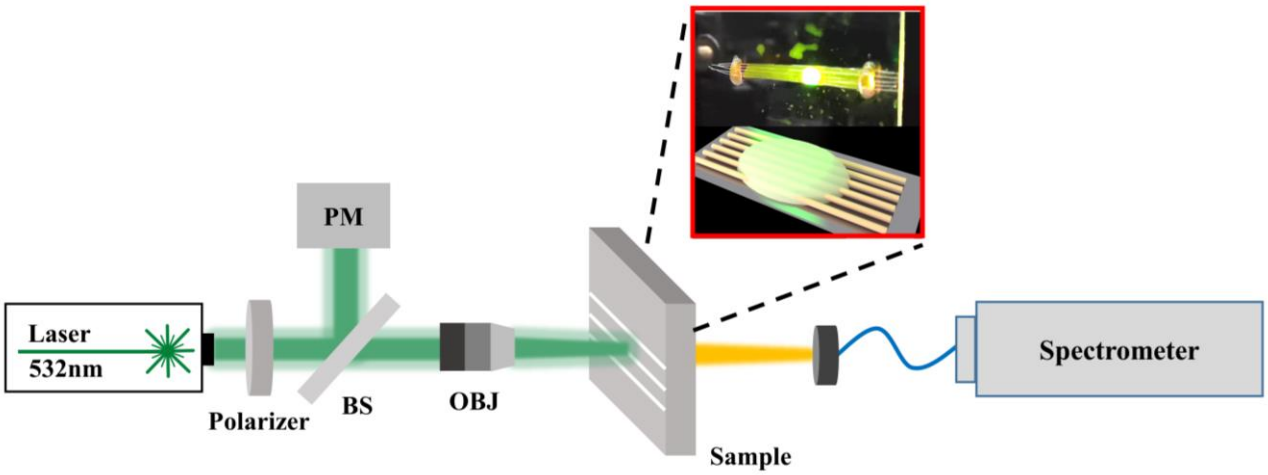

Figure 1. Schematic of the experimental setup. BS, beam splitter. PM, power meter. OBJ, objective. The green lines represent the pump light trajectory, while the portion of the laser output received by the spectrometer (the upper half of the inset within the red box is the actual image of the sample, and the lower half is a schematic diagram for sample).

3. Results

3.1. Regular WGM Lasing

The flexible optical fibers are arranged into a transverse array with an average center-to-center spacing of 150 μm (i.e., sample I in the inset of Figure 2a). The average spacing is greater than $(d_p + D)$. Figure 2a shows that sample I exhibits the fluorescence spectrum of spontaneous emission at low pump power. As the pump power increases, evenly spaced sharp peaks gradually appear in the spectrum, which is a typical characteristic of WGM lasing. Figure 2b presents the output power (orange-colored) and linewidth (purple-colored) of the laser as a function of pump power. With the increase in pump power, the output power initially grows slowly but later rises rapidly, while the full width at half maximum (FWHM) of the output spectrum decreases quickly from 35 nm and maintains below 1 nm. This indicates that the threshold for stable WGM output is 3.15 mJ/cm^2. Additionally, the WGM spectrum is analyzed at a pump energy of 3.7 mJ/cm^2 in Figure 2c. The center wavelength is 576 nm, and the FSR is 1.1 nm. The theoretical value of the FSR is $\Delta\lambda = \frac{\lambda^2}{n_{eff} \cdot \pi D} \approx 1.115$ nm ($\lambda = 576$ nm is the resonance wavelength, $D = 60$ μm is the diameter of the micropillar, and $n_{eff} \approx 1.58$ is the effective refractive index) [44], which agrees well with the experimental results. Furthermore, Figure 2d shows the power Fourier transform (PFT) [45] of the output spectrum at a pump energy of 3.7 mJ/cm^2. The PFT exhibits a distinct peak at 188.1 μm, corresponding to the characteristic cavity length ($L = \pi D = 188.5$ μm) of the WGM output.

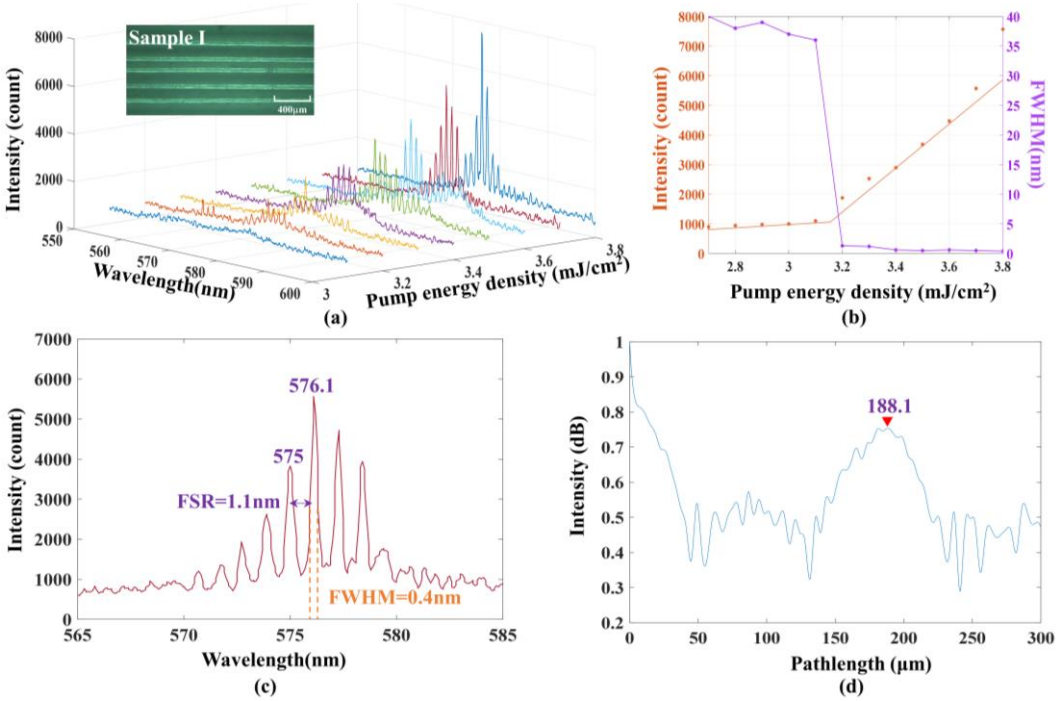

Figure 2. Output of sample I, the regular WGM laser. (**a**) Output spectra at different pump intensity (the inset shows experimental image of sample I with an average spacing of 150 μm between neighbor fibers); (**b**) output power (orange) and linewidth (purple) of the WGM lasing versus pump intensity (solid circles represent experimental data, and the solid line indicates the fitting result); (**c**) output spectrum when pump intensity is 3.7 mJ/cm^2 (the purple bidirectional arrow represents FSR, and the orange dashed lines represents FWHM); (**d**) PFT diagram of the WGM laser (the vertical axis is on a normalized logarithmic scale).

3.2. Random WGM Lasing

The average center-to-center spacing of the flexible fiber array is changed from 150 μm to a range of less than 10 μm (i.e., sample II in the inset of Figure 3a). The average spacing is less than $(d_p + D)$. Figure 3a shows that the output spectrum transitions from the spontaneous fluorescence spectrum to an unusual lasing spectrum with the pump power increasing. Figure 3b presents the output power (in orange) and linewidth (in purple) of the laser as a function of pump power density. It shows that the lasing threshold of sample II is approximately 3.02 mJ/cm^2, which is a bit lower than that of sample I. We infer that this is due to the more compact structure of sample II, which provides stronger confinement of the liquid gain medium as well as stronger coupling between neighbor fibers/lasers, thereby improving pump efficiency and lowering the threshold. When pump power is at 3.55 mJ/cm^2 the output spectrum is also analyzed in Figure 3c. It can be observed that the peak envelope of the longitudinal modes in the output spectrum no longer exhibits a Gaussian-like distribution but instead shows strong chaotic behavior, similar to that of random lasers. The calculated FSR fluctuates between 0.9 nm and 1.2 nm, which is attributed to the coupling of individual WGM lasers in the fiber array through evanescent fields. This coupling results in intense mode competition and possible interference effects, both of which lead to redistribution and random fluctuations of the spectral amplitude. Nevertheless, the peak positions remain relatively fixed within a certain wavelength range (as analyzed later), showing the characteristic of fixed mode spacing of WGMs supported by the flexible fibers. Based on the above characteristics, we name it R-WGM laser. The corresponding spectral PFT shows several peaks, corresponding to multiple resonances cavities with different lengths, as shown in Figure 3d. In order to gain

a deeper understanding of this interesting phenomenon, further experiments and analyses were conducted.

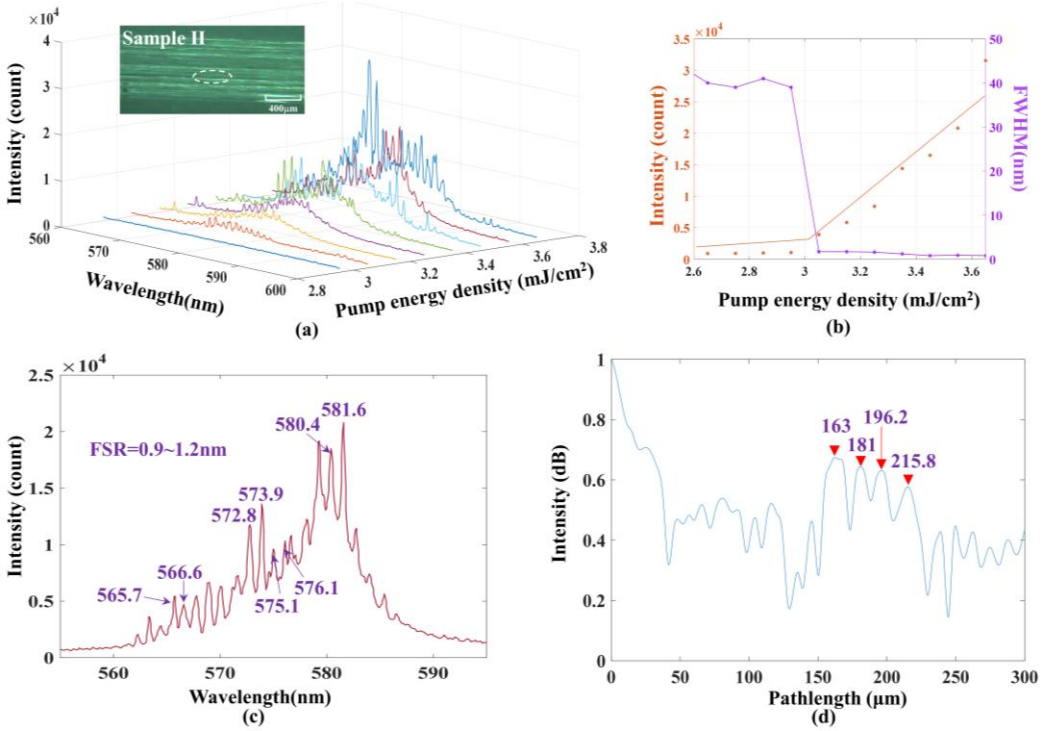

Figure 3. Output of sample II, the random WGM laser. (**a**) Output spectra at different pump intensity (the inset shows experimental image of sample II with an average spacing of less than 10 μm, as indicated by the dashed box); (**b**) output power (orange) and linewidth (purple) of the R-WGM lasing versus pump intensity (solid circles represent experimental data, and the solid line indicates the fitting result); (**c**) output spectrum when pump intensity is 3.55 mJ/cm^2; (**d**) PFT diagram of the R-WGM laser (the vertical axis is on a normalized logarithmic scale).

3.3. Comparison Between the Two Lasing Regimes

A stability analysis of the laser output under the two different emission regimes is performed. Using the same pump power, multiple pulses are applied to the same sample, and the excitation spectra of sample I and sample II are sequentially recorded shot-by-shot. The output spectral envelope of sample I formed by wide-spread fibers remains stable across different pulses, with the mode emission position unchanged, as shown in Figure 4a,c. In contrast, the output spectral envelope of sample II formed by narrow-spread fibers exhibits significant random fluctuations, with the mode emission position almost unchanged, as shown in Figure 4b,d. The photodegradation effect of the gain solution in sample I is observed [46,47], which causes a slight decrease in output intensity with increasing pump cycles. However, this phenomenon is not evident in sample II. This is attributed to regular WGM corresponding to only a few relatively fixed resonant modes, and the dye molecules along these paths undergoing relatively more cycles of energy absorption and release, which results in a more pronounced photodegradation effect. In contrast, each pulse excites random WGM with significant variation, meaning that each pulse activates resonant modes along different paths. This leads to a wider range of dye molecules participating in the resonance, thereby alleviating the photodegradation effect. This reflects that random WGMs can utilize the gain medium more efficiently. In Figure 4c, the two output spectra under different pump periods are highly overlapped and exhibit a relatively low spectral baseline, indicating a stable and pure WGM emission. In contrast, Figure 4d shows that the peak position of R-WGM lasing under different pump periods slightly diverge (wavelength shift of less than 0.4 nm is observed), as marked by triangles

and the dashed box. The slight wavelength shifts are responsible for the non-constant FSR of the R-WGM, as shown in Figure 3c.

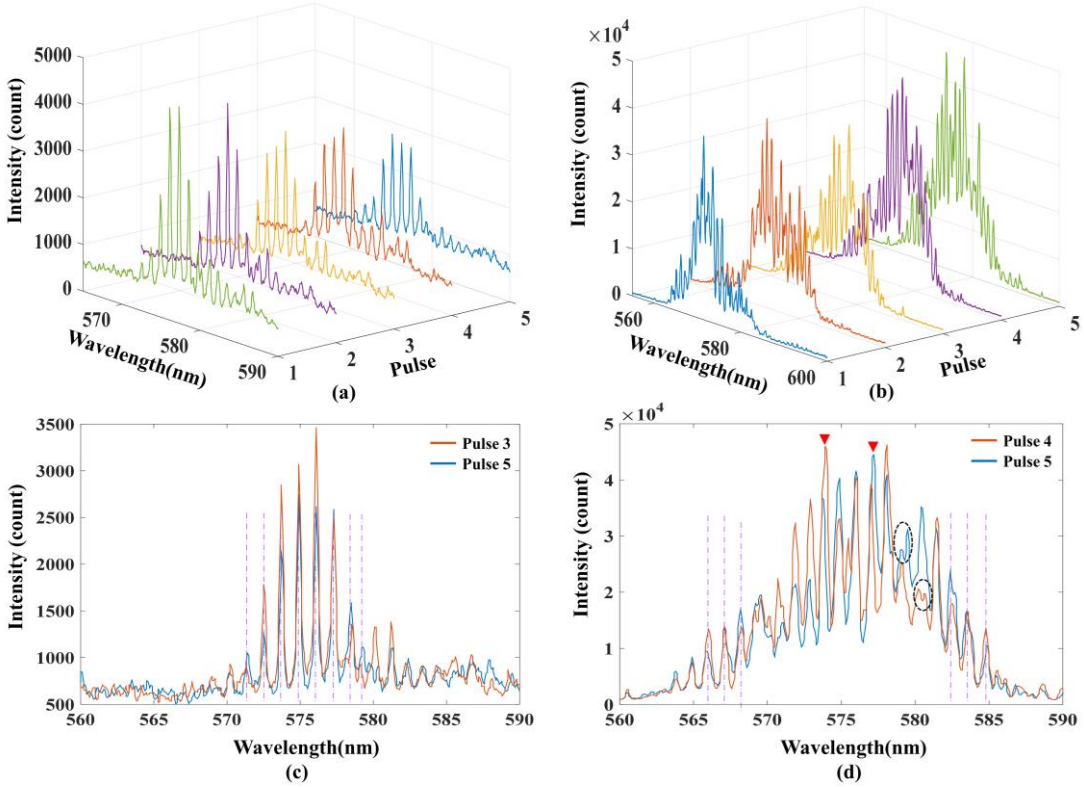

Figure 4. Stability analysis of the output spectra in different pulse periods. (**a**) Regular WGM emission of different shots of pulses; (**b**) R-WGM output of different shot of pulses; (**c**) detailed comparison of regular WGM output between different shots of pulses (mode-overlap positions are marked by dashed lines); (**d**) detailed comparison of R-WGM output between different shots of pulses (mode-overlap positions are marked by dashed lines, deviations by triangles, and mode splitting by elliptical dashed lines).

The PFT corresponding to different R-WGM output spectra are investigated in Figure 5a,b. By combining Figure 3d, it can be observed that the laser path of the R-WGM is no longer fixed around the flexible fiber's circumference under different pulses, but instead follows multiple random paths, corresponding to several equivalent cavity lengths that randomly deviate from the standard cavity length of 188.5 μm. We infer that this is due to the proximity of the flexible fiber, where the evanescent fields (the maximum penetration depth is 81 μm) of different WGM modes couple with each other, leading to significant field injection and leakage between degenerate WGM modes. This further promotes the excitation of specific modes corresponding to specific paths, which exhibit a gain advantage. Additionally, the more compact fiber microcavity structure results in the excitation of new WGM modes corresponding to new paths between adjacent fiber walls (manifesting as instability in the FSR and cavity length), thus exhibiting the multi-peak phenomenon in the PFT. In Figure 5c,d, the peaks corresponding to the fundamental, second, and third standard pathlength (approximately 180 μm, 360 μm, and 520 μm) are observed in the PFT spectrum, and the corresponding intensities decrease as the pathlength increases. Interestingly, around the integer multiples of the standard pathlength, there are several peaks with intensities noticeably higher than the surrounding ones, forming "pathlength bands" in clusters (green dashed line). This further suggests that random WGM lasing results from a combination of various complex mechanisms.

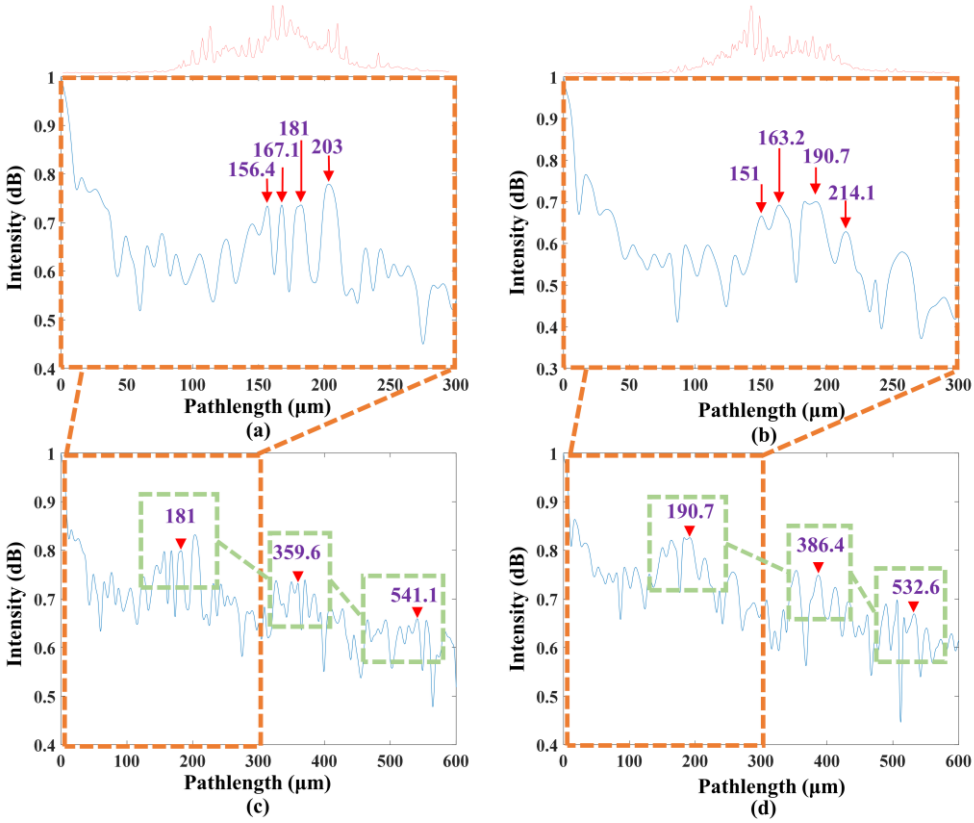

Figure 5. The PFT of two specific spectra of the R-WGM output (the vertical axis is on a normalized logarithmic scale). (**c**) and (**d**) represent two different random WGM states, while (**a**,**b**) are magnified views of the orange dashed portions of (**c**,**d**), respectively. The green dashed line indicates the region where the peaks are collectively concentrated.

4. Encryption Application Based on the R-WGM

Due to the output spectrum exhibiting multiple resonant peaks and significant fluctuations in both the FSR and peak amplitude, the modes and amplitudes of the R-WGM laser are difficult to predict. This unpredictability allows it to generate encryption keys or sequences that are more complex and unpredictable than traditional pseudorandom numbers, thereby enhancing the security of information encryption. In addition, compared to traditional key generators, the keys generated by R-WGM lasers can remain unpredictable and unclonable across multiple dimensions, such as time (different pulse batches) and space (different array spacings). This characteristic makes encryption based on R-WGM lasers more reliable and stable.

Based on the advantages mentioned above, we designed a simple RSA authentication application based on the R-WGM, as shown in Figure 6. The Certifying Authority (denoted as *C*) collects the spectrum output from the R-WGM laser and quantizes it into binary bits according to a specified amplitude threshold. *C* groups the generated bitstream into pairs, denoted as p^{id_i} and q^{id_i}, where i indicates the group index. *C* selects the public key $e = 65537$ (the default constant of the algorithm) and publishes it. Using the RSA algorithm, *C* generates the corresponding modulus n and private key d for each group using e, p^{id_i}, and q^{id_i} [48]. When Alice wants to prove the reliability of the message M (e.g., "Alice is a dentist") sent to Bob, she seeks certification from *C* (a trusted third party for Alice and Bob). Alice sends the message M to *C*. Upon receiving M, *C* randomly selects an id, such as $id = 2$, from its groups. Due to the one-way and compressive nature of hash functions, typically only the hash of the message is signed. Therefore, *C* computes the hash value $h(M)$ (e.g., "8B42…") and signs it with the private key d as $\sigma = h(M)^d \ mod \ n$, and

subsequently publishes the signature σ. Upon receiving the signature σ, Bob calculates $h(M)^* = \sigma^e \ mod \ n$ using the public key e. If $h(M)^* = h(M)$, Bob believes that C has authenticated the message M ("Alice is a dentist").

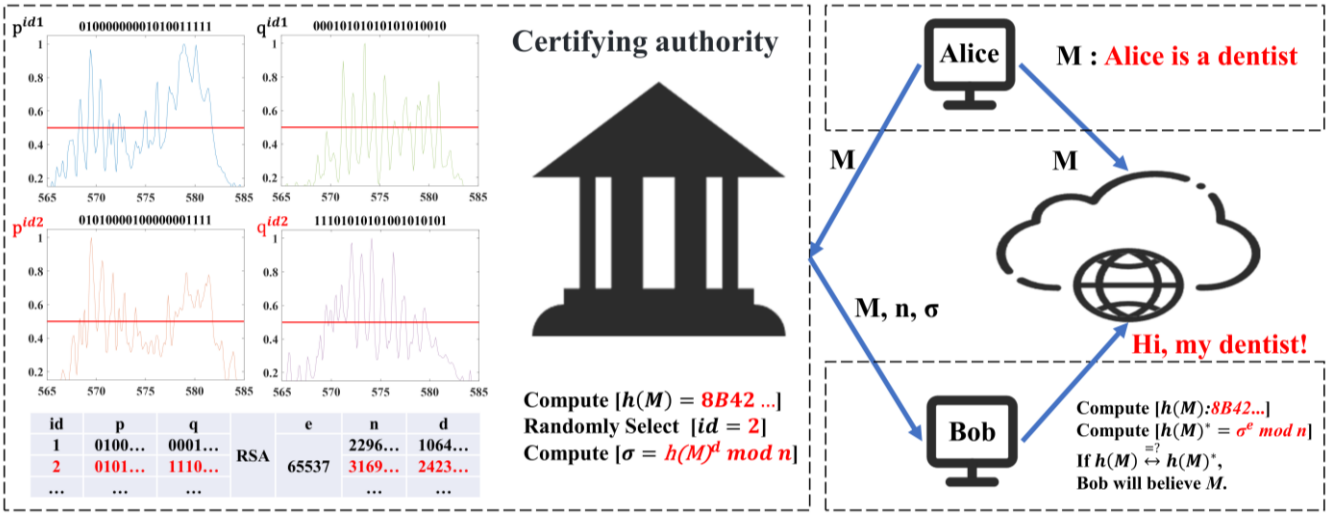

Figure 6. RSA authentication application based on the R-WGM.

It is worth noting that since the RSA algorithm is based on the properties of the Integer Factorization Problem, it is difficult for an adversary to forge a signature σ that satisfies the $h(M)^* = h(M)$ verification requirement, unless they know d. Compared with traditional RSA signature authentication, RSA authentication based on R-WGM is more reliable. This is because the p^{id_i} and q^{id_i} used to generate the private key d are derived from a true random number generator, which inherits the fluctuation of the R-WGM spectrum output. Furthermore, the broadband characteristics of the spectrum corresponding to more bits further enhance the attack resistance of the private key d.

5. Discussion

Compared to other types of micro-lasers, this laser based on a flexible fiber array has the following advantages: First, its random lasing with varying pathlength effectively delays the photodegradation effect of the gain dye observed in fixed-path lasing, enhancing the gain utilization and thereby extending its lifespan. This improves, to some extent, the stability of the laser's single-output power, enabling it to perform well in power-sensitive applications [49,50]. At the same time, the fiber used in the experiment (which is far from meeting experimental-grade requirements) is much cheaper than typical commercial optical fibers, significantly reducing the manufacturing and application costs. Moreover, by simply adjusting the spacing between the array elements, the randomness of the laser output can be controlled, providing a simple means for observing the mechanisms of complex WGM modes [51]. Furthermore, as a random microcavity fiber laser, its narrow linewidth and random spectral output make it an ideal and easily deployable light source for super-resolution detection, compressed sensing, and other applications [52,53]. Finally, this article leaves several aspects open for future exploration. For instance, the coupling output direction from the fiber array could be further optimized, and macroscopic control of the cavity structure to enhance the laser's directional coupling still requires investigation. The spatial and temporal characteristics of the laser output may also reveal additional interesting features. Many experimental phenomena are analyzed qualitatively, and while the article presents new ideas for random laser generation, it lacks deeper quantitative modeling.

6. Conclusions

In this article, control over the complex lasing mechanism of the fiber microcavity is achieved through the precise design of the average spacing in a flexible polyamide optical fiber array, which modifies the coupling relationships between different WGM modes within the array. This modification results in the transition of the microcavity's lasing modes from standard WGM to R-WGM. Further stability experiments demonstrate that, despite strong envelope fluctuations in the R-WGM output spectrum, the intrinsic properties of WGM emission are still preserved. Finally, based on the characteristics of the R-WGM output spectrum, including instability and broad linewidth, it is employed as a true random number generator for RSA signature authentication, thereby enhancing the key's resistance to attacks.

Author Contributions: Conceptualization, all authors; methodology, B.C. and Z.H.; software, B.C. and Z.H.; validation, B.C. and Z.H.; formal analysis, all authors; investigation, all authors; resources, Z.H.; data curation, Z.H.; writing—original draft preparation, B.C.; writing—review and editing, Z.H. and W.Z.; visualization, Z.H. and B.C.; supervision, W.Z.; project administration, W.Z.; funding acquisition, W.Z. All authors have read and agreed to the published version of the manuscript.

Funding: This work was supported in part by the National Natural Science Foundation of China (Grant Nos. 62375040 and 11974071).

Institutional Review Board Statement: Not applicable.

Informed Consent Statement: Not applicable.

Data Availability Statement: Data underlying the results presented in this paper could be obtained from the authors upon reasonable request, for example, if you are interested in collaborating with us in the fields of random lasers and optical microcavity construction, or in conducting more in-depth research in these areas.

Conflicts of Interest: The authors declare no conflicts of interest.

References

1. Vahala, K.J. Optical Microcavities. *Nature* **2003**, *424*, 839–846. [CrossRef] [PubMed]
2. Xiao, Y.-F.; Gong, Q. Optical Microcavity: From Fundamental Physics to Functional Photonics Devices. *Sci. Bull.* **2016**, *61*, 185–186. [CrossRef]
3. Ge, L.; Feng, L.; Schwefel, H.G.L. Optical Microcavities: New Understandings and Developments. *Photon. Res.* **2017**, *5*, OM1. [CrossRef]
4. Yang, K.Y.; Oh, D.Y.; Lee, S.H.; Yang, Q.-F.; Yi, X.; Shen, B.; Wang, H.; Vahala, K. Bridging Ultrahigh-Q Devices and Photonic Circuits. *Nat. Photon.* **2018**, *12*, 297–302. [CrossRef]
5. Huang, S.-H.; Su, H.-P.; Chen, C.-Y.; Lin, Y.-C.; Yang, Z.; Shi, Y.; Song, Q.; Wu, P.C. Microcavity-Assisted Multi-Resonant Metasurfaces Enabling Versatile Wavefront Engineering. *Nat. Commun.* **2024**, *15*, 9658. [CrossRef]
6. Fu, W.; Wu, H.; Feng, M. Superconducting Processor Modulated VCSELs for 4K High-Speed Optical Data Link. *IEEE J. Quantum Electron.* **2022**, *58*, 1–8. [CrossRef]
7. Cao, X.; Yang, H.; Wu, Z.-L.; Li, B.-B. Ultrasound Sensing with Optical Microcavities. *Light. Sci. Appl.* **2024**, *13*, 159. [CrossRef]
8. Hao, Y.-Z.; Sheng, M.-W.; Zhang, Z.-N.; Li, J.-C.; Xiao, J.-L.; Yang, Y.-D.; Huang, Y.-Z. High-Speed Directly Modulated Widely Tunable Hybrid Square/Rhombus-Rectangular Coupled Cavity Lasers. *J. Light. Technol.* **2023**, *41*, 5668–5674. [CrossRef]
9. Wu, Y.; Duan, B.; Li, C.; Yang, D. Multimode Sensing Based on Optical Microcavities. *Front. Optoelectron.* **2023**, *16*, 29. [CrossRef]
10. Yu, D.; Humar, M.; Meserve, K.; Bailey, R.C.; Chormaic, S.N.; Vollmer, F. Whispering-Gallery-Mode Sensors for Biological and Physical Sensing. *Nat. Rev. Methods Primers* **2021**, *1*, 1–22. [CrossRef]
11. Chen, Z.; Xu, Q.; Zhang, K.; Wong, W.-H.; Zhang, D.-L.; Pun, E.Y.-B.; Wang, C. Efficient Erbium-Doped Thin-Film Lithium Niobate Waveguide Amplifiers. *Opt. Lett.* **2021**, *46*, 1161. [CrossRef] [PubMed]
12. Jiang, S.; Zhou, H.; Liu, C.; Gu, Z.; Zhang, N. Mode Selection and Unidirectional Emission in Multiple-Deformed Microcavity through Dynamic Tunneling. *Opt. Laser Technol.* **2024**, *169*, 110070. [CrossRef]
13. Li, M.; Tian, M.; Lin, C.; Chen, S.; Feng, Z.; Tan, Y. Microcavity Raman Laser-Based FMCW LiDAR with Enhanced Echo Sensitivity. *ACS Photonics* **2024**, *11*, 801–809. [CrossRef]

14. Yang, J.; Qin, T.; Zhang, F.; Chen, X.; Jiang, X.; Wan, W. Multiphysical Sensing of Light, Sound and Microwave in a Microcavity Brillouin Laser. *Nanophotonics* **2020**, *9*, 2915–2925. [CrossRef]
15. Zhu, H.Y.; Zhang, J.C.; Zhang, W.L. Photothermal Effect Controlled Complex Lasing for Decentralized Key Distribution. *ACS Photonics* **2022**, *9*, 3600–3608. [CrossRef]
16. Bitarafan, M.; DeCorby, R. On-Chip High-Finesse Fabry-Perot Microcavities for Optical Sensing and Quantum Information. *Sensors* **2017**, *17*, 1748. [CrossRef]
17. Robinson, J.T.; Chen, L.; Lipson, M. On-Chip Gas Detection in Silicon Optical Microcavities. *Opt. Express* **2008**, *16*, 4296–4301. [CrossRef]
18. Wachter, G.; Kuhn, S.; Minniberger, S.; Salter, C.; Asenbaum, P.; Millen, J.; Schneider, M.; Schalko, J.; Schmid, U.; Felgner, A.; et al. Silicon Microcavity Arrays with Open Access and a Finesse of Half a Million. *Light. Sci. Appl.* **2019**, *8*, 37. [CrossRef]
19. Chen, Y.; Yin, Y.; Ma, L.; Schmidt, O.G. Recent Progress on Optoplasmonic Whispering-Gallery-Mode Microcavities. *Adv. Opt. Mater.* **2021**, *9*, 2100143. [CrossRef]
20. Houghton, M.C.; Kashanian, S.V.; Derrien, T.L.; Masuda, K.; Vollmer, F. Whispering-Gallery Mode Optoplasmonic Microcavities: From Advanced Single-Molecule Sensors and Microlasers to Applications in Synthetic Biology. *ACS Photonics* **2024**, *11*, 892–903. [CrossRef]
21. Duan, R.; Zhang, Z.; Xiao, L.; Zhao, X.; Thung, Y.T.; Ding, L.; Liu, Z.; Yang, J.; Ta, V.D.; Sun, H. Ultralow-Threshold and High-Quality Whispering-Gallery-Mode Lasing from Colloidal Core/Hybrid-Shell Quantum Wells. *Adv. Mater.* **2022**, *34*, 2108884. [CrossRef] [PubMed]
22. Yang, X.; Tang, S.-J.; Meng, J.-W.; Zhang, P.-J.; Chen, Y.-L.; Xiao, Y.-F. Phase-Transition Microcavity Laser. *Nano Lett.* **2023**, *23*, 3048–3053. [CrossRef] [PubMed]
23. Zhu, X.; He, Z.; Zhu, H.; Zhang, W. Spectrally Programmable Fiber Microcavity Laser with Dye-Doped Liquid Crystals. *Opt. Laser Technol.* **2023**, *158*, 108860. [CrossRef]
24. Wang, P.; Wang, Y.; Yang, Z.; Guo, X.; Lin, X.; Yu, X.-C.; Xiao, Y.-F.; Fang, W.; Zhang, L.; Lu, G.; et al. Single-Band 2-nm-Line-Width Plasmon Resonance in a Strongly Coupled Au Nanorod. *Nano Lett.* **2015**, *15*, 7581–7586. [CrossRef]
25. Fu, Y.; Qing, Y.M.; Li, Z.; Zayats, A.V.; Lei, D. Tale of Two Resonances: Waveguide–Plasmon Coupling and High *Q*.-Factor Engineering on the Nanoscale. *ACS Photonics* **2023**, *10*, 2–12. [CrossRef]
26. Yang, X.; Gong, C.; Zhang, C.; Wang, Y.; Yan, G.-F.; Wei, L.; Chen, Y.-C.; Rao, Y.-J.; Gong, Y. Fiber Optofluidic Microlasers: Structures, Characteristics, and Applications. *Laser Photonics Rev.* **2022**, *16*, 2100171. [CrossRef]
27. Zhu, S.; Shi, L.; Xiao, B.; Zhang, X.; Fan, X. All-Optical Tunable Microlaser Based on an Ultrahigh-*Q*. Erbium-Doped Hybrid Microbottle Cavity. *ACS Photonics* **2018**, *5*, 3794–3800. [CrossRef]
28. Kong, L. Room-Temperature near-Infrared Whispering-Gallery-Mode Lasing from Two-Dimensional CdSe Microplates. *J. Mater. Chem. C* **2021**, *9*, 9222–9228. [CrossRef]
29. Salehzadeh, O.; Djavid, M.; Tran, N.H.; Shih, I.; Mi, Z. Optically Pumped Two-Dimensional MoS2 Lasers Operating at Room-Temperature. *Nano Lett.* **2015**, *15*, 5302–5306. [CrossRef]
30. Zhu, H.; He, Z.; Wang, J.; Zhang, W.; Pei, C.; Ma, R.; Zhang, J.; Wei, J.; Liu, W. Microcavity Complex Lasers: From Order to Disorder. *Ann. Phys.* **2024**, *536*, 2400112. [CrossRef]
31. Peccianti, M.; Pasquazi, A.; Park, Y.; Little, B.E.; Chu, S.T.; Moss, D.J.; Morandotti, R. Demonstration of a Stable Ultrafast Laser Based on a Nonlinear Microcavity. *Nat. Commun.* **2012**, *3*, 765. [CrossRef] [PubMed]
32. Wang, S.; Liu, S.; Liu, Y.; Xiao, S.; Wang, Z.; Fan, Y.; Han, J.; Ge, L.; Song, Q. Direct Observation of Chaotic Resonances in Optical Microcavities. *Light. Sci. Appl.* **2021**, *10*, 135. [CrossRef] [PubMed]
33. Makhonin, M.; Delphan, A.; Song, K.W.; Walker, P.; Isoniemi, T.; Claronino, P.; Orfanakis, K.; Rajendran, S.K.; Ohadi, H.; Heckötter, J.; et al. Nonlinear Rydberg Exciton-Polaritons in Cu2O Microcavities. *Light. Sci. Appl.* **2024**, *13*, 47. [CrossRef] [PubMed]
34. Yi, X.; Yang, Q.-F.; Yang, K.Y.; Vahala, K. Imaging Soliton Dynamics in Optical Microcavities. *Nat. Commun.* **2018**, *9*, 3565. [CrossRef]
35. Liu, W.; Tang, S.-J.; Xiao, Y.-F. Nonlinear Optical Microcavities Towards Single-Molecule Sensing. In *Single Molecule Sensing Beyond Fluorescence*; Bowen, W., Vollmer, F., Gordon, R., Eds.; Springer International Publishing: Cham, Switzerland, 2022; pp. 97–123, ISBN 978-3-030-90339-8.
36. Chen, N.; Liu, C.; Lu, Z.; Tao, W.; Peng, M. Femtosecond Laser Processing for a High Sensitivity Fiber MZI Microcavity. *Opt. Express* **2022**, *30*, 12397–12408. [CrossRef]
37. Di Donato, A.; Pietrangelo, T.; Anzellotti, A.; Monti, T.; Morini, A.; Farina, M. Infrared Imaging in Liquid through an Extrinsic Optical Microcavity. *Opt. Lett.* **2013**, *38*, 5094. [CrossRef]
38. Di Donato, A.; Criante, L.; LoTurco, S.; Farina, M. Optical Microcavity Scanning 3D Tomography. *Opt. Lett.* **2014**, *39*, 5495. [CrossRef]
39. Guo, J.; Rao, Y.; Zhang, W.; Cui, Z.; Liu, A.; Yan, Y. Dental Imaging With Near-Infrared Transillumination Using Random Fiber Laser. *Photonic Sens.* **2020**, *10*, 333–339. [CrossRef]

40. Hu, Z.; Zhang, Q.; Miao, B.; Fu, Q.; Zou, G.; Chen, Y.; Luo, Y.; Zhang, D.; Wang, P.; Ming, H.; et al. Coherent Random Fiber Laser Based on Nanoparticles Scattering in the Extremely Weakly Scattering Regime. *Phys. Rev. Lett.* **2012**, *109*, 253901. [CrossRef]
41. Lin, J.-H.; Huang, J.-W.; Wu, J.-J.; Tsay, S.-Y.; Chen, Y.-H. Electrically Controllable Random Lasing from Dye-Doped Nematic Liquid Crystals within a Capillary Fiber. *Opt. Mater. Express* **2018**, *8*, 2910. [CrossRef]
42. Wang, Z.; Cao, M.; Shao, G.; Zhang, Z.; Yu, H.; Chen, Y.; Zhang, Y.; Li, Y.; Xu, B.; Wang, Y.; et al. Coherent Random Lasing in Colloidal Quantum Dot-Doped Polymer-Dispersed Liquid Crystal with Low Threshold and High Stability. *J. Phys. Chem. Lett.* **2020**, *11*, 767–774. [CrossRef] [PubMed]
43. Tabassum, R.; Kant, R. Recent Trends in Surface Plasmon Resonance Based Fiber–Optic Gas Sensors Utilizing Metal Oxides and Carbon Nanomaterials as Functional Entities. *Sens. Actuators B Chem.* **2020**, *310*, 127813. [CrossRef]
44. Krasnokutska, I.; Tambasco, J.-L.J.; Peruzzo, A. Tunable Large Free Spectral Range Microring Resonators in Lithium Niobate on Insulator. *Sci. Rep.* **2019**, *9*, 11086. [CrossRef] [PubMed]
45. Hofstetter, D.; Thornton, R.L. Loss Measurements on Semiconductor Lasers by Fourier Analysis of the Emission Spectra. *Appl. Phys. Lett.* **1998**, *72*, 404–406. [CrossRef]
46. Bañuelos Prieto, J.; López Arbeloa, F.; Martínez Martínez, V.; Arbeloa López, T.; López Arbeloa, I. Photophysical Properties of the Pyrromethene 597 Dye: Solvent Effect. *J. Phys. Chem. A* **2004**, *108*, 5503–5508. [CrossRef]
47. Tanaka, N.; Sisk, W.N. The Photodegradation of Pyrromethene 567 and Pyrromethene 597 by Pyrromethene 546. *J. Photochem. Photobiol. A Chem.* **2005**, *172*, 109–114. [CrossRef]
48. Kaliski, B. RSA Digital Signature Scheme. In *Encyclopedia of Cryptography and Security*; van Tilborg, H.C.A., Ed.; Springer: Boston, MA, USA, 2005; pp. 527–531, ISBN 978-0-387-23483-0.
49. Abedin, K.M.; Al Jabri, A.R.; Mujibur Rahman, S.M. Power Stability of Different Lasers and Its Effect on the Outcome of Phase-Stepping Shearography Experiments. *Results Opt.* **2023**, *12*, 100490. [CrossRef]
50. Vahlbruch, H.; Wilken, D.; Mehmet, M.; Willke, B. Laser Power Stabilization beyond the Shot Noise Limit Using Squeezed Light. *Phys. Rev. Lett.* **2018**, *121*, 173601. [CrossRef]
51. Niu, L.; Li, X.; Fang, Z.; Zhang, W.; Xie, K.; Zhang, T.; Huang, H.; Wang, G.; Zhang, J.; Hu, Z.; et al. Random Lasers with Controlled Emission Modes by Colloidal Semiconductor Quantum Dots Coupled to Plasmonic Nanorod Arrays. *Opt. Laser Technol.* **2025**, *180*, 111430. [CrossRef]
52. Boschetti, A.; Taschin, A.; Bartolini, P.; Tiwari, A.K.; Pattelli, L.; Torre, R.; Wiersma, D.S. Spectral Super-Resolution Spectroscopy Using a Random Laser. *Nat. Photonics* **2020**, *14*, 177–182. [CrossRef]
53. Gomes, A.S.L.; Moura, A.L.; De Araújo, C.B.; Raposo, E.P. Recent Advances and Applications of Random Lasers and Random Fiber Lasers. *Prog. Quantum Electron.* **2021**, *78*, 100343. [CrossRef]

Disclaimer/Publisher's Note: The statements, opinions and data contained in all publications are solely those of the individual author(s) and contributor(s) and not of MDPI and/or the editor(s). MDPI and/or the editor(s) disclaim responsibility for any injury to people or property resulting from any ideas, methods, instructions or products referred to in the content.